



POLITECNICO
MILANO 1863

RE.PUBLIC@POLIMI

Research Publications at Politecnico di Milano

Post-Print

This is the accepted version of:

M. Belan, L. Arosti, R. Polatti, F. Maggi, S. Fiorini, F. Sottovia
A Parametric Study of Electrodes Geometries for Atmospheric Electrohydrodynamic Propulsion

Journal of Electrostatics, Vol. 113, 2021, 103616 (8 pages)
doi:10.1016/j.elstat.2021.103616

The final publication is available at <https://doi.org/10.1016/j.elstat.2021.103616>

Access to the published version may require subscription.

When citing this work, cite the original published paper.

© 2021. This manuscript version is made available under the CC-BY-NC-ND 4.0 license
<http://creativecommons.org/licenses/by-nc-nd/4.0/>

Permanent link to this version

<http://hdl.handle.net/11311/1183017>

A parametric study of electrodes geometries for atmospheric electrohydrodynamic propulsion

Marco Belan^{a,*}, Luca Arosti^a, Riccardo Polatti^a, Filippo Maggi^a, Samuele Fiorini^b,
Federico Sottovia^b

^a*Politecnico di Milano, Dipartimento di Scienze e Tecnologie Aerospaziali, 20156 Milano, Italia*

^b*SF2, 37045 Legnago (VR), Italia*

Abstract

This work presents a parametric analysis of corona thrusters performance as function of electrodes geometry, focusing on collector electrodes. A set of airfoil-shaped collectors with fixed chord and different profiles is tested on a propulsion system at bench. The setup consists in a parallel array of thruster units with adjustable spacing. The downstream velocity field is measured and used to determine thrust by momentum balance. Thrust-to-power ratio and thrust density are calculated as performance parameters to compare the different geometries. Optimal configurations are found within the examined parameter space, evidencing the importance of further systematic studies about the electrodes geometries.

Keywords: corona discharge, atmospheric EHD propulsion, corona electrodes

1. Introduction

Nowadays, a growing trend towards the reduction of fossil fuel use is pushing the interest in electrical propulsion technologies powered by advanced Li-ion batteries, solar panels, fuel cells [1, 2, 3] or an optimal combination of the former ones. The performance in terms of efficiency, energy density and durability of said energy carriers grows consistently attracting the interest of all fields requiring a portable power source.

Electrohydrodynamic (EHD) propulsion would permit to exploit recent advances in these technologies for atmospheric flight, also providing several other advantages such as absence of moving parts and low noise production. The first devices which exploited EHD propulsion were called lifters [4]. Their structure is rather simple: usually triangle-shaped, presenting a small diameter conductive wire hold tense above a vertical aluminum foil so that one of its thin edges is facing the wire. Everything is kept together by a light non-conducting structure. Powered by keeping a sufficiently high voltage between wire and

*Corresponding Author

Email address: marco.belan@polimi.it (Marco Belan)

foil, these simple devices exploit corona effect to create an ionic wind. They showed the capability to lift their own weight but not the power source, which is kept on ground. A variety of applications of this principle is available in literature, including different kinds of thruster and even an EHD propeller able to lift off without being tethered to the voltage source [5]. The most recent flying devices prove to have reached a technology level much higher than the first lifters: in particular, Khomich and Rebrov [6] presented a vertical take-off ionocraft with wireless power source, and Xu et al. [7] created a light model aircraft propelled by EHD thrusters, able to fly at steady level carrying its power generation system.

EHD thrusters produce propulsive force generating ions which drift between two electrodes, exchanging momentum with the neutral air. The fundamental component of an EHD propulsion system is the thruster unit, which is composed by two electrodes, an emitter and a collector separated by a gap and connected to a high voltage source. The emitter is the one with the smallest curvature radius, where ion production happens thanks to the high surrounding electric field giving rise to non-equilibrium or cold plasma. The collector presents a larger frontal area, it is typically much larger than the emitter and the ionic wind around it creates a significant aerodynamic drag [8]. When two thruster units are placed one above the other, they form a thruster cell, as shown in Fig. 1. Besides the gap distance d between emitter and collector, this configuration introduces the spacing s as a further parameter. Under the same physical principles, in other similar geometries the emitters are placed on intermediate positions between subsequent collectors [6], and also dual stage thrusters with an intermediate electrode between emitter and collector have been considered [9].

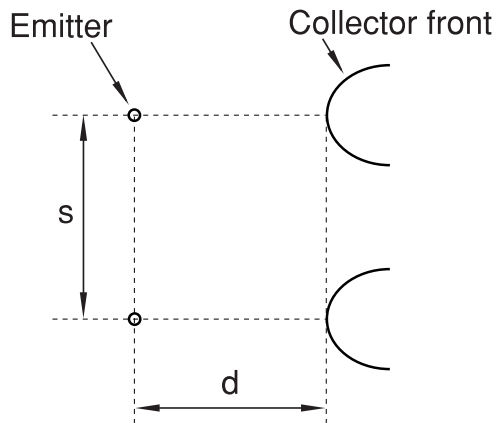


Figure 1: Thruster cell drawing with main geometrical parameters: gap d , spacing s . The emitters size is enlarged for clarity.

Performance of these kind of thrusters is quite remarkable, and further improvements are expected since thrust-to-power ratios larger than 100 N/kW were already measured as peak values in laboratory by Masuyama and Barrett [9], whilst the value for a typical jet

aircraft engine is in the order of 2 N/kW. The above mentioned work presents a theoretical model which gives in absence of drag an EHD thrust

$$T = \frac{I d}{\mu}, \quad (1)$$

where I is the current flowing through the electrodes, d the gap distance and μ the ion mobility. Introducing the power absorption P , Eq. (1) leads to express the thrust-to-power ratio as

$$\Theta = \frac{T}{P} = \frac{d}{\mu V} \quad (2)$$

where V is the voltage applied between the electrodes. Besides thrust and thrust-to-power, another important performance indicator is the thrust density, that can be defined as the ratio between the thrust produced by the propulsion system and its frontal area or volume. Recently, more detailed models have also appeared, giving the chance of estimating the performance indicators accounting for corona ignition voltage and aerodynamic drag [10].

The literature reports several studies devoted to performance optimization by varying electric parameters such as voltage and polarity as well as geometric parameters including for example gap and spacing. Multistage and array configurations were tested systematically in order to study their performance [11], proving that when multiple thruster units are operated together, the thrust worsens when the units are too close to each other while the thrust density obviously decreases when the units are widely spaced. Thrust and thrust-to-power increase by using a DBD discharge as alternative method to corona effect for ion production, at the cost of an increased complexity of the thruster design [12]. Large gaps were proven to increase thrust-to-power according to Eq. (1) but only if accounting for leakage currents and reverse corona effect [13]. Performance in a rarefied atmosphere is also currently being studied [14].

With few exceptions, however, the above mentioned works take into account the simplest electrodes geometry, which consists in a wire as emitter and a metal cylinder as collector electrode [15]. Despite this configuration being simple to build and test, none of the few state of the art devices that achieved sustained flight up to date used such a geometry. Indeed, the mentioned aeroplane [7] mounted a two-stage corona thruster array with wires as positive emitters and standard symmetric airfoils as collectors, while the ionocraft [6] used wires as negative emitters and drop-shaped collectors arranged in an array.

The aim of the present work is to provide a parametric analysis of corona thrusters performance as function of the electrodes geometry, considering that different shapes for the collector electrodes have been employed in literature. A wide body of results is available for the cylindrical collectors, however their aerodynamic drag is definitely large. On the other hand, there are examples of airfoil-shaped collectors with low drag but a systematic study about their geometry is not available.

For the above reasons, the present investigation focuses on a set of airfoil-shaped collectors with fixed chord and different shapes and thicknesses, in order to study how

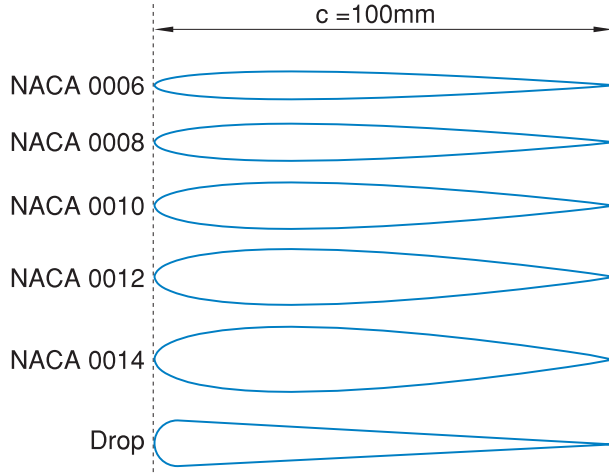


Figure 2: Airfoil profiles of the collectors under test, to scale.

the performance depends on the combined effects of different ionic winds and drag forces, which are both affected by shape and maximum thickness (or frontal area) of the collectors. The setup is based on a parallel array of thrusters with adjustable spacing distance, and the flow field created by the thruster array is described by velocity measurements, carried out by means of a pitot probe downstream of the collectors trailing edges. Thrust, thrust-to-power and thrust density are then obtained from data processing and used to compare the different geometries, in order to obtain a data set which could serve as starting point for future optimizations in view of the design of new devices.

2. Experimental Setup

The propulsive system considered in this work consists in five identical thruster units, each composed by an emitter and a collector electrode, positioned one above the other as in Fig. 1 with the same spacing s . The number of units was chosen in order to approximate periodic conditions around the central unit, where the measurements are made.

Preliminary tests of the system were done by using a single kind of collectors and varying both the gap d and the spacing s [16]. With a fixed voltage of 20 kV, the gap was varied between 20 and 30 mm obtaining an electric field well above corona ignition and below electrical arcing. The dependence on gap was found to be qualitatively in accordance with scaling laws (1) and (2), suggesting to focus the present investigation on the less studied effects of shape and spacing of the collectors. Thus, in order to complete the present experimental campaign in a reasonable time, in this work the gap was set to a constant value $d = 20$ mm, which gives in the present setup a relatively high electric field and produces output velocities in a good range for measurements. The parameter space considered here is defined by the spacing range s together with the collectors geometries, as explained below and in results section.

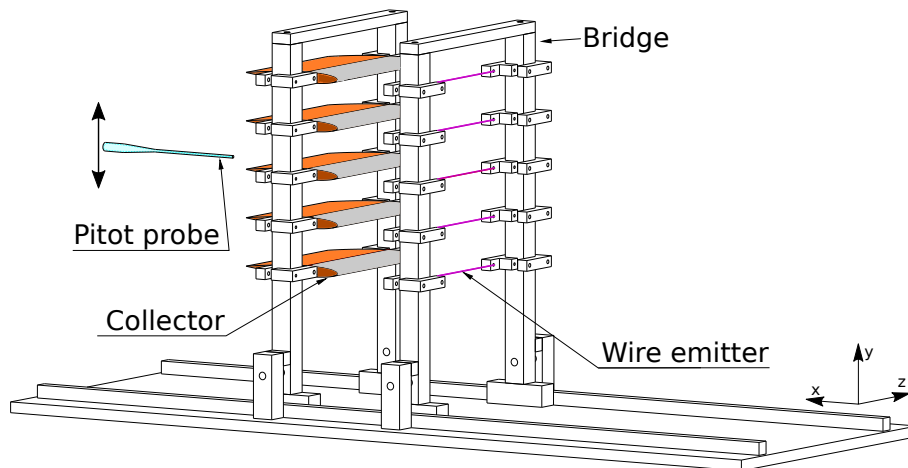


Figure 3: Drawing of the test bench with five thruster units mounted. The reference frame is shown on the right.

The emitters (anodes) are connected to a positive high voltage source and the collectors (cathodes) are connected to ground. The emitters, which remain unchanged for every configuration, are $30 \mu\text{m}$ diameter constantan wires with 110 mm of exposed length, along which corona effect is developed. Several collector electrodes with different aerodynamic profiles are tested, all characterized by the same chord $c = 100 \text{ mm}$ and span $b = 140 \text{ mm}$. In particular, six symmetric airfoil-shaped collectors have been produced, namely NACA 0006, 0008, 0010, 0012, 0014 and a drop-shaped profile, all sketched in Fig. 2. The NACA airfoils (standard airfoil shapes defined by the National Advisory Committee for Aeronautics) were chosen because of their promising performance in recent literature [7, 10], selecting for this experiment a reasonable thickness range (6 to 14 mm or $0.06 c$ to $0.14 c$). The drop airfoil, well studied and successfully used in literature [6, 17, 18], is defined as a profile with semicircular leading edge tapered with straight lines to a sharp trailing edge. In the present experiment, this airfoil was produced after testing the NACA set, choosing for the drop shape the same thickness of the best performing NACA airfoil. In this way, a direct comparison was done between the best NACA and a drop airfoil having the same thickness and chord.

The experimental setup is based on a custom built test rig designed to accommodate several thruster units with variable spacing and gap distances. A drawing of the support structure with five thruster units mounted is presented in Fig. 3. The support structure, made entirely of polymethylmethacrylate (PMMA) in order to avoid insulation problems, consists in a base capable of accommodating two or more bridges, whose vertical columns serve as supports for the electrodes; for the purpose of this work, only two bridges are mounted, each one of frontal area $200 \times 355 \text{ mm}^2$. The base is 300mm wide and 800mm long, with screwed rails which provide a sliding coupling with the bridges.

The collectors are made of 3D-printed acrylonitrile butadiene styrene (ABS) polymer,

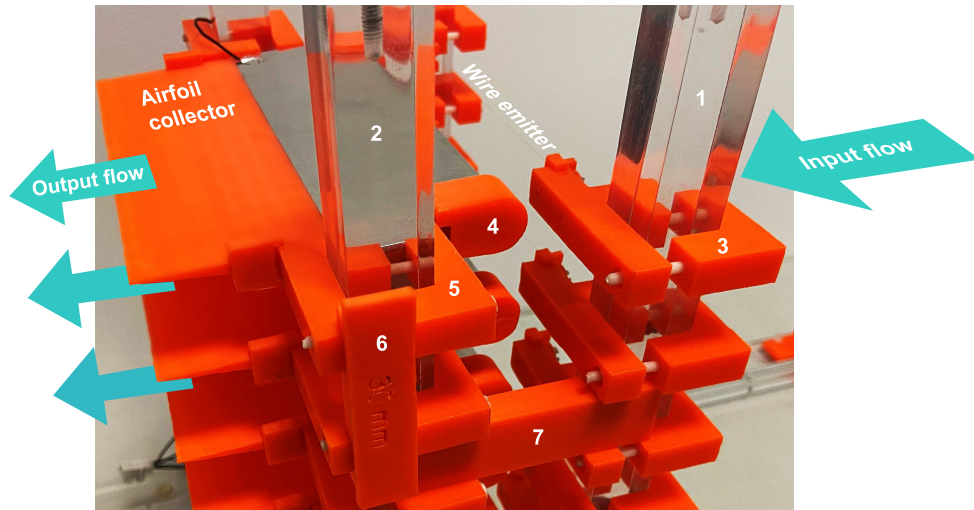


Figure 4: Details of the thrusters assembly: 1) fore bridge; 2) aft bridge; 3) emitter clamp; 4) collector cap; 5) collector clamp; 6) t-shaped spacing clip; 7) gap clip.

with the frontal part coated by a 0.075 mm thickness aluminium tape with a chordwise extension of 70 mm along the surface. The lateral sides of the leading edge are protected by 3D-printed ABS caps because of the local intensification of the electric field. On both the lateral sides, adjustable ABS clamps lock the collectors at the bridge columns at the desired height. The couplings are designed in order to minimize misalignments caused by mechanical backlash. Emitters are held by clamps through nylon screws that also allow mechanical tension adjustment. Two different sets of t-shaped clips have been realized, the first one in order to set the desired gap distance and the second one to adjust thruster units spacing correctly. The mechanical details are shown in Fig. 4.

All experiments are performed in a rectangular test chamber which is 0.41 m wide, 0.41 m high and 1 m deep. Right and left walls are made of insulating materials, while floor and ceiling are made of metal. A fine screen with 1.6 mm cells is positioned on the inlet in order to limit aerodynamic disturbances in the incoming flow. On the outlet, another screen with coarse mesh (35 mm) is installed for safety reasons. All the components of the test chamber made of conductive material are grounded for safety reasons and to reduce electric disturbances.

Flow velocity is measured by means of a pitot probe, in this experiment a thin pipe made of Pyrex with an internal diameter of 0.5 mm and an external one of 1.2 mm. Probe dimensions were chosen to guarantee a good spatial resolution and to minimize aerodynamic interference with the flow. The probe is sustained by an insulating support rigidly connected to a 2D traversing system that permits to explore vertical sections of the field of motion downstream of the cathodes, with a positioning accuracy of ± 0.1 mm. Pressure between capillary tip and external reference is measured by a differential transducer with range 0 to 10 Pa and accuracy of $\pm 0.1\%$ of the full scale.

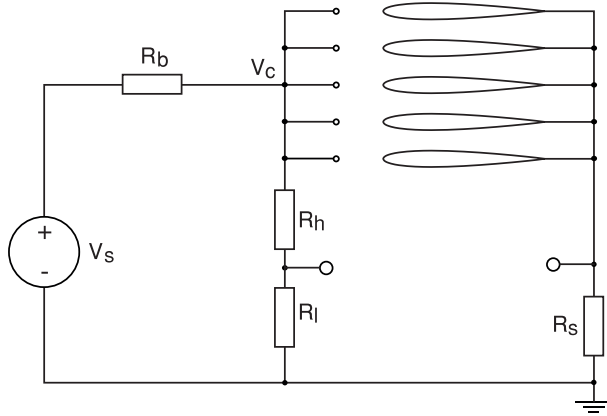


Figure 5: Electric circuit scheme.

Fig. 5 represents a schematic of the electric circuit. During the tests, a positive DC voltage $V_s = 20$ kV is provided to the wires through a common ballast resistance R_b of 1.00 M Ω , while the coated airfoils are grounded. The voltage drop across R_b is in the order of 0.5 kV during normal operation and increases only in the event of a malfunction. Even the high voltage supply is equipped with a safety circuit to protect the instrument in case of spark appearance.

Electrical quantities directly measured during tests are total current flowing in the circuit I_{tot} and voltage between electrodes V_c . I_{tot} is normally measured by means of the ammeter integrated in the power supply unit, with an accuracy of ± 0.005 mA. In addition, in some tests a shunt resistance $R_s = 470$ Ω was employed in series with the collectors in order to directly measure I_{tot} at high sampling rates, confirming ammeter readings and the presence of a stable glow regime. V_c measurements are performed exploiting a voltage divider in parallel with the corona electrodes, with a total resistance $R_l + R_h = 152.9$ M Ω and an output voltage ratio of 10^{-4} . The resulting uncertainty is about ± 30 V on an average value of V_c of tens of kilovolts applied to the thruster system.

A typical test consists in a set of pressure measurements performed at various stations along the vertical centerline downstream of the thruster units. Average values of the temporal series with their standard deviations are used to determine the velocity with the relevant fluctuations for every vertical station. Concerning electric measurements, since the thrusters worked in the same conditions during all the pressure measurements for a fixed value of geometric parameters, mean values are obtained by averaging over all the temporal series acquired at every station of the pitot. In the standard acquisition procedure, data from the analog output of the pressure transducer and the voltage divider are recorded by an oscilloscope, using a time window of 20 s at 40 kSamples/s. In high speed acquisitions for detailed electric measurements, the voltage divider and shunt signals are recorded by the same oscilloscope on 2 s time windows at 2.5 GSamples/s.

2.1. Velocity measurements

Velocity measurements are performed 2 mm downstream of the thrusters, with vertical steps Δy between 0.5 mm and 1 mm. For each configuration, the velocity profiles are measured around the central unit in order to properly represent the periodicity of the output flow, and in particular along a thruster cell between two consecutive trailing edges above or below the central collector. The velocity of the airflow is evaluated exploiting Bernoulli theorem

$$p_{tot} = p_s + \frac{1}{2}\rho u^2, \quad (3)$$

where the static pressure p_s at measurement locations is equal to the ambient pressure and the pressure transducer reads the difference $p_{tot} - p_s$. Air density ρ is obtained from room temperature and pressure using the perfect gas law. Variations in air density due to humidity were found negligible in the laboratory environment, therefore they were not taken into account. The probe works in conditions of low Reynolds number, thus a correction method is applied to the velocity calculations. Probe Reynolds number is defined as:

$$Re_{d_P} = \frac{d_P u}{\nu}, \quad (4)$$

where d_P is the probe outer diameter, u the local flow speed and ν is the kinematic viscosity. When Re_{d_P} is low, indicatively below 10^3 , the effect of viscosity is to increase the measured impact pressure, hence the measured velocity, above the true value. Therefore, the acquired values were corrected by the method of Zagarola and Smits [19].

Assuming uncorrelated uncertainties with symmetrical distribution for the instruments, Root Sum Squared (RSS) method was applied to compute the propagation of errors on the velocities. This gives a lower bound for the velocity uncertainty, in the order of ± 0.015 m/s (1σ). However, as shown later in the results section, the inherent fluctuations of the velocity field can reach amplitudes much larger than the above uncertainty, since the Reynolds number of the output flow

$$Re = \frac{c \bar{u}}{\nu} \quad (5)$$

based on chord c and mean flow velocity \bar{u} , is high enough to give rise to partially developed turbulence.

2.2. Thrust calculation

Thrust forces were estimated for every geometric configuration starting from experimental velocity profiles. Since measurements were performed moving along the upright direction on the vertical plane positioned on the cathode mid-span chord, where the flow could be considered two-dimensional, the thrust forces obtained at the end of this section

are to be considered per unit span. Calculations were performed by exploiting momentum conservation equation for a stationary flow:

$$\iint_{\mathcal{S}} \rho \mathbf{u} (\mathbf{u} \cdot \mathbf{n}) d\mathcal{S} = \mathbf{F}_{\text{visc}} - \iint_{\mathcal{S}} p \mathbf{n} d\mathcal{S} + \iiint_{\mathcal{V}} \rho_q \mathbf{E} d\mathcal{V} , \quad (6)$$

where \mathcal{S} is the surface of the control volume \mathcal{V} , \mathbf{n} its normal vector, p the pressure acting on the external surfaces of the control volume, ρ and \mathbf{u} density and velocity, \mathbf{F}_{visc} represents the viscous forces, ρ_q the space charge density and \mathbf{E} the electric field. The terms can be further divided by distinguishing forces acting on the collectors surface (subscript c) from the ones acting on the free boundaries (subscript b):

$$\mathbf{F}_{\text{visc}} = \mathbf{F}_{\text{visc},\mathcal{S}_b} + \mathbf{F}_{\text{visc},\mathcal{S}_c} , \quad (7)$$

$$\iint_{\mathcal{S}} p \mathbf{n} d\mathcal{S} = \iint_{\mathcal{S}_b} p \mathbf{n} d\mathcal{S} + \iint_{\mathcal{S}_c} p \mathbf{n} d\mathcal{S} . \quad (8)$$

Forces acting on the 30 μm wires are not considered because negligible with respect to the ones acting on the 100 mm chord collectors, as confirmed also by numerical simulations [18]. External viscous forces acting on the free surfaces can also be neglected, because viscosity effects are relevant only near the solid walls of the domain. Eq. (6) now becomes:

$$\iint_{\mathcal{S}} \rho \mathbf{u} (\mathbf{u} \cdot \mathbf{n}) d\mathcal{S} = \mathbf{F}_{\text{visc},\mathcal{S}_c} - \iint_{\mathcal{S}_c} p \mathbf{n} d\mathcal{S} + \iiint_{\mathcal{V}} \rho_q \mathbf{E} d\mathcal{V} - \iint_{\mathcal{S}_b} p \mathbf{n} d\mathcal{S} . \quad (9)$$

The sum of aerodynamic forces acting on \mathcal{S}_c and the electrostatic forces is the net force $-\mathbf{T}$ experienced by the thruster, and is represented by the first 3 terms on the right hand side:

$$\iint_{\mathcal{S}} \rho \mathbf{u} (\mathbf{u} \cdot \mathbf{n}) d\mathcal{S} = -\mathbf{T} - \iint_{\mathcal{S}_b} p \mathbf{n} d\mathcal{S} \quad (10)$$

(formally, in the reference frame \mathbf{T} is the force on the fluid along the x direction and $-\mathbf{T}$ the one exerted by the fluid on the thruster assembly). Taking the horizontal component of the equation, and considering line integrals instead of surface ones (2D assumption), the thrust force per unit span can be written as function of the momentum flow and the pressure forces

$$-\frac{T}{b} = \int_{\mathcal{L}} \rho \mathbf{u} \cdot \mathbf{x} (\mathbf{u} \cdot \mathbf{n}) d\mathcal{L} + \int_{\mathcal{L}_b} p \mathbf{n} \cdot \mathbf{x} d\mathcal{L} , \quad (11)$$

where \mathbf{x} is the unit vector parallel to the cathode chord directed as the centerline flow velocity.

For this periodic propulsion system, the considered control volume represents one thruster cell and is sketched in Fig. 6. It presents boundaries on the two facing surfaces of two subsequent cathodes and on the streamlines that end on the respective leading edges. Outlet area is delimited by two adjacent collector trailing edges, but can be at an

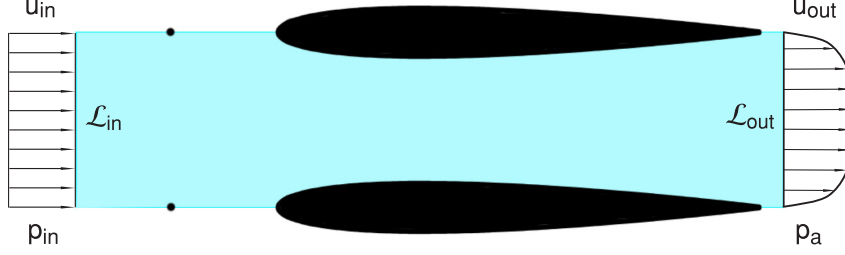


Figure 6: Control volume used for thrust calculation.

arbitrary location downstream of the cell. The selected location for outlet area is the one where velocity measurements were taken. The inlet area is equal to the outlet one, but located upstream of the anode wires. The flow is considered, for periodicity reasons, to enter the drifting zone aligned with \mathbf{x} . For this reason, the momentum flow integral can be simplified:

$$\int_{\mathcal{L}} \rho \mathbf{u} \cdot \mathbf{x} (\mathbf{u} \cdot \mathbf{n}) d\mathcal{L} = \int_{\mathcal{L}_{out}} \rho u^2 d\mathcal{L} - \int_{\mathcal{L}_{in}} \rho u^2 d\mathcal{L} . \quad (12)$$

The quantity $u|_{\mathcal{L}_{out}}$ is known from velocity profiles measurements, while $u|_{\mathcal{L}_{in}}$ can be represented by a constant value u_{in} estimated by continuity conditions applied between inlet and outlet surfaces, both of span b :

$$\rho u_{in} b s = b \int_{\mathcal{L}_{out}} \rho u d\mathcal{L} . \quad (13)$$

Since upstream of the thruster the flow is accelerated from a condition of zero velocity and ambient pressure, the inlet area just before the drifting zone will be at a pressure slightly lower than the ambient. Since the exit jet is in pressure equilibrium with the ambient, this pressure difference contributes to increase the developed thrust. Considering constant pressure along the inlet and outlet areas, the thrust of Eq. (11) can now be expressed as

$$-\frac{T}{b} = \int_{\mathcal{L}_{out}} \rho u^2 d\mathcal{L} - \int_{\mathcal{L}_{in}} \rho u^2 d\mathcal{L} + (p_a - p_{in}) |\mathcal{L}_{out}| , \quad (14)$$

where p_a represents the ambient pressure, p_{in} is the pressure at the control volume inlet and the quantity $|\mathcal{L}_{out}| = |\mathcal{L}_{in}| = s$ is the height of the inlet and outlet sections. p_{in} was estimated starting from Bernoulli theorem accounting for the pressure loss due to the air flowing through the inlet screen of the test section

$$p_{in} = p_a - \frac{1}{2} \rho u_{in}^2 - K \frac{1}{2} \rho u_{ts}^2 , \quad (15)$$

where K is the pressure loss coefficient of the screen and u_{ts} is the flow velocity at the test chamber inlet section, where the screen is positioned. Its value was estimated assuming

that, for periodicity reasons, the same mass flow entering a cell section of area bs (span \times spacing) passes through a screen portion of area ls , where l is the width of the screen and of the test chamber. Assuming a constant u_{ts} on the relevant area ls , this gives $\rho u_{ts}ls = \rho u_{in}bs$ and

$$u_{ts} = u_{in} \frac{b}{l} \quad (16)$$

Inlet speeds values were also checked by means of an hot film anemometer, showing good consistency with the assumption above.

The thrust evaluated by Eq.(14) relies on simplifying assumptions as exposed above, however the comparison of different geometries, which is the aim of the present work, can only be marginally affected by these assumptions since the same algorithm is always used to evaluate the performance of the different collectors.

3. Results

3.1. Parameter space

The explored parameter space is defined by the variations of collector shapes and of spacing s . By observing that when the thruster units are too close to each other the performance is generally affected in a negative way, and that for large spacings the thruster units tend to behave as independent isolated units, a spacing range was defined between $s = 20$ mm and $s = 40$ mm, i.e. $0.2c \leq s \leq 0.4c$. By setting 5 points on this interval (20, 25, 30, 35, 40 mm) with 6 collectors shapes, the corresponding number of tests is 30. Additional tests were introduced by adding in some cases the spacing values 22.5 and 27.5 mm, in the range where the system properties exhibit the larger variations, bringing the total number of tests to 35. In each test, a velocity profile was acquired for a central cell and then used to determine thrust according to §2.2. At the same time the power consumption was measured. In turn, these values were used to obtain thrust-to-power ratio and thrust density. Further 6 tests were performed on single isolated thrusters (one for each collector shape) in order to characterize their behaviour when they are not assembled in a periodic structure.

3.2. Velocity profiles

Velocity profiles are obtained by averaging data both in time and from multiple measurements (20 s repeated up to 5 times), and are presented in a dimensionless form, using spacing s as scaling factor for the vertical displacement y and assuming as reference velocity the mean value generated by a single thrusting unit under ideal conditions without viscous effects:

$$u_{ref} = \sqrt{\frac{I d}{\rho \mu b s}} \quad (17)$$

The resulting u_{ref} values range from 1.68 to 2.17 m/s depending on the spacing s . The error bars on the data are represented with a confidence level of 1σ in terms of standard

deviation, and represent the total variations superimposed to the average values including both the random errors and the physical fluctuations due to the flow regime. Since the Reynolds number ranges up to $2 \cdot 10^4$, the resulting regime can be defined as partially developed turbulence, and it is easy to see that turbulent fluctuations can be much larger than errors due to the instruments uncertainty, even if the pitot-pipe-transducer system has a low-pass response, limited to few Hz.

The average velocities curves were interpolated using the least square method in order to obtain analytical expressions useful for subsequent integrations. The chosen interpolator is a superposition of gaussian functions, which can properly represent the trends resulting from experimental data:

$$u(y) = a + b e^{-h(y-k)^2} + \sum_{i=1}^2 c_i [e^{-d_i(y-e_i-k)^2} + e^{-d_i(y+e_i-k)^2}] \quad (18)$$

The curve is forced to be symmetrical around the point $y = k$, as can be easily seen from Eq. (18). All asymmetries in measurements have been regarded as caused by small mounting misalignments, considered as a source of systematic experimental error.

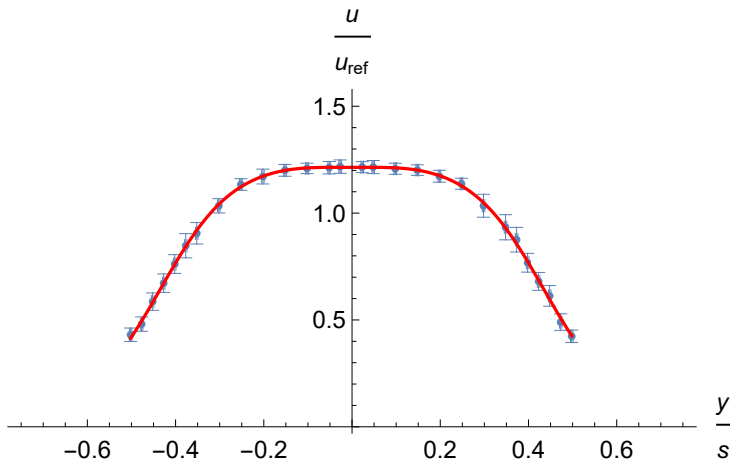


Figure 7: Thruster cell dimensionless velocity profile for NACA 0010 airfoil, spacing $s = 20$ mm. $y/s = \pm 0.5$ and $y/s = 0$ represent respectively collectors trailing edges and cell center height.

For small spacing values, where blockage effects becomes dominant, the velocity profiles downstream of a cell exhibit a channel-like behaviour as in Fig. 7. This profile is more pronounced when thick collectors are tested. When spacing is increased the flow gradually shifts towards a double jet behaviour, with a minimum in the cell center and two symmetric maxima, as in Fig. 8. For particularly thin collectors, such as NACA 0006 and 0008, no channel-like behaviour was ever observed during the tests.

The error bars in Figs. 7 and 8 include the turbulent fluctuations in order to give more information in a compact way about the regime of the output flow. The fluctuations

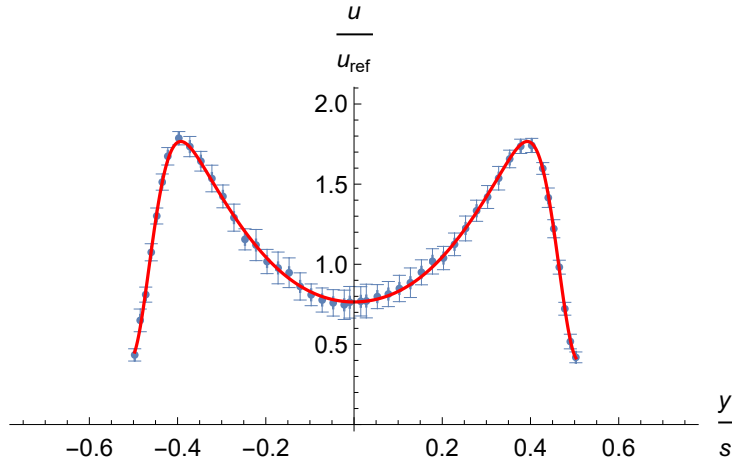


Figure 8: Thruster cell dimensionless velocity profile for NACA 0012 airfoil, spacing $s = 40$ mm. $y/s = \pm 0.5$ and $y/s = 0$ represent respectively collectors trailing edges and cell center height.

intensity is generally low on channel-like profiles with narrow spacings and for the thicker airfoils the observed flow becomes stable enough to presume laminar conditions. On the other hand, the largest fluctuations were observed in the central zone of the double jet profiles, as visible in Fig. 8. This phenomenon could be interpreted as turbulent diffusion of momentum from the fast lateral jets toward the central zone. A different behavior was observed for the drop collectors, which exhibit a laminar behavior almost independent of spacing.

3.3. Thrust-to-power ratio

Thrust-to-power ratio $\Theta = T/P$ is calculated referring to thrust obtained as in §2.2 and power consumption obtained from current and voltage measurements. Since power P showed only small uncorrelated variations during the tests of different collector geometries, all power consumption data has been exploited to identify a common trend for power P as function of spacing s . This trend, visible in Fig. 9, indicates a slow power increase for larger spacings, and assuming that P tends to an asymptotic value for $s \rightarrow \infty$ when the units are so far each other to vanish any interaction, a general interpolation function was introduced as follows:

$$P(s) = a_P(1 - c_P e^{-t_P s}), \quad (19)$$

where a_P , c_P and t_P are least square optimization parameters. The blue lines in Fig. 9 show the interpolating function and its 2σ confidence interval. The resulting function has been used to fit power consumption for every collector geometry.

For all the collectors under test, also the thrust-to-power ratios turn out to increase with growing spacings, tending to asymptotic saturation values characteristic of single thruster units. This indicates that even for this quantity a fit of the kind

$$\Theta(s) = a_\Theta(1 - c_\Theta e^{-t_\Theta s}) \quad (20)$$

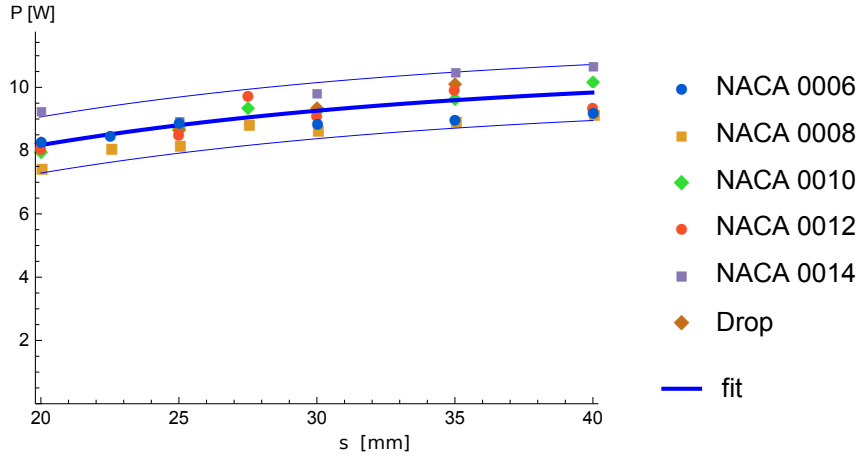


Figure 9: Power consumption curve.

is appropriate, however with specific a_θ , c_θ and t_θ for each collector geometry. The existence of saturation values consistent with the fits (19) and (20) was confirmed by measuring thrust and power on single thruster units for all the tested geometries.

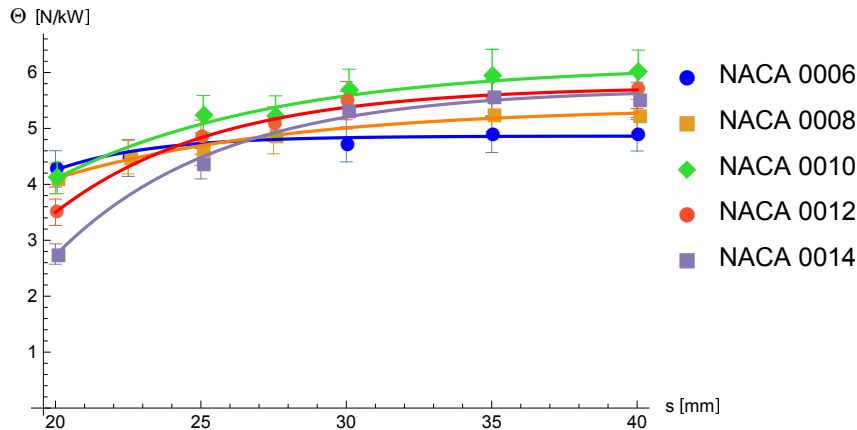


Figure 10: Thrust-to-power ratios curves for the NACA airfoil set.

Figure 10 presents thrust-to-power ratios for all the NACA shapes under test, with 1σ error bars and fitting functions of the kind (20) compatible with the data. It is found that for small spacings, where aerodynamic blockage effects are more important, thin collectors give higher Θ values. The thicker collectors perform better for large spacings but create larger drags; as a trade-off, the NACA 0010 electrodes present the best performance, particularly if higher spacing are considered.

In Fig. 11 the NACA 0010 are also compared with drop shaped collectors having same thickness and chord, and the NACA 0010 present higher Θ almost for every value of s , with the only exception of the short spacing $s = 20 \text{ mm}$.

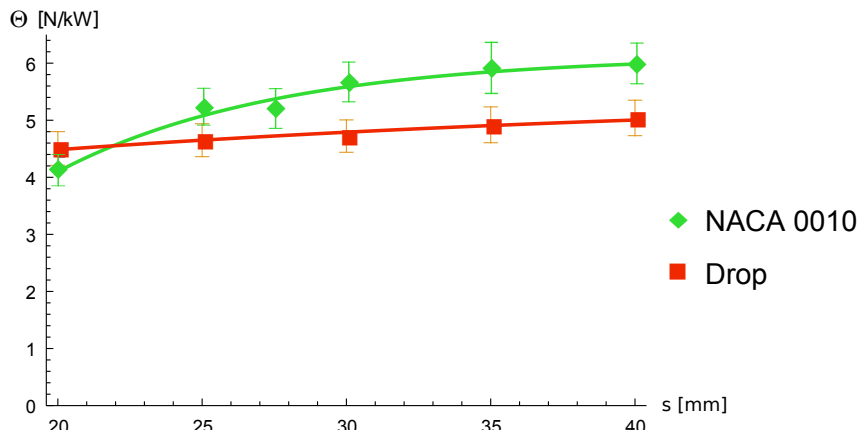


Figure 11: Thrust-to-power ratio curves for NACA 0010 and drop collectors.

3.4. Thrust density

Thrust density can be defined in relation to propulsion system frontal area, Ψ_A , or total volume, Ψ_V :

$$\Psi_A = \frac{T}{A} = \frac{T}{s b}, \quad (21)$$

$$\Psi_V = \frac{T}{V} = \frac{T}{s b L}, \quad (22)$$

where $L = d + c$ is the sum of gap and electrodes chord. Since volumetric thrust density can be written as $\Psi_V = \Psi_A/L$ and L is constant during the present tests, only results for Ψ_A are shown in what follows. Fig. 12 represents thrust density for NACA shaped collectors as function of s , with 1σ error bars. Solid lines are obtained using a fitting function of the form

$$f(s) = \frac{a_\Psi(1 - c_\Psi e^{-t_\Psi s})}{s}, \quad (23)$$

which accounts for the decrease of Ψ_A for increasing s , since in this limit the thrust tends to a constant (independent units) and the area $A = bs$ grows linearly.

Most geometries show a common behaviour, with a maximum located among the tested range. For smaller spacings, Ψ_A should decrease because of the growing blockage and obviously tend to zero when the collectors touch each others: this effect is more pronounced with thicker collectors. On the other hand, it is clear that Ψ_A decreases also for large spacings, and this justifies the presence of a local maximum. Fig. 12 shows also that an increase in collector thickness moves the maximum towards higher spacing values. The greatest Ψ_A value is obtained for NACA 0010 collectors with spacing $s = 25$ mm = $0.25 c$: a check of the starting data shows that this collector benefits from a thrust generally slightly larger than the others over the spacing interval under study, and this acts on both ratios $\Psi_A = T/A$ and $\Theta = T/P$.

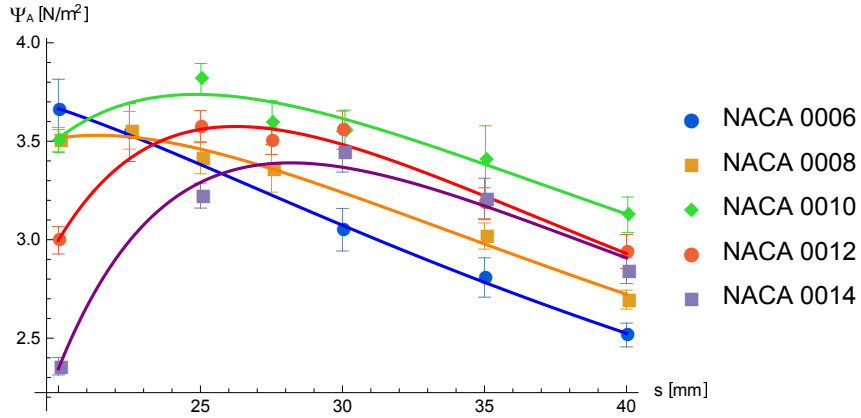


Figure 12: Thrust density curves for NACA airfoil collectors.

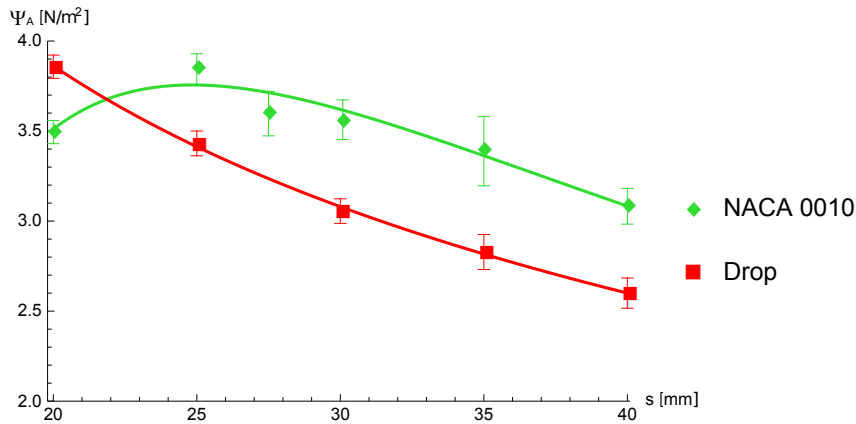


Figure 13: Thrust Density curves for NACA 0010 and drop collectors.

In Fig. 13, NACA 0010 and drop electrodes with same thickness and chord are compared. The drop electrodes show a monotonic decreasing rate with increasing s , however for small spacing values the thrust density has a better performance than NACA 0010 and the presence of a local maximum at smaller s can not be excluded, but this condition corresponds to lower thrust-to-power ratios (Fig. 11) and high drag.

3.5. Configuration design diagrams

An overview of the above results which could be exploited for EHD thrusters design can be obtained by plotting for different collectors thrust-to-power ratios Θ versus thrust densities Ψ_A as parametric curves on the spacing s . This is done for the NACA set in Fig. 14, where each line represents $[\Theta(s), \Psi_A(s)]$ for a different collector, with arrows that evidence the direction of increasing spacing s . For the NACA 0010, 0012 and 0014 collectors, the relevant curves show an increase in thrust-to-power ratio and thrust density for low spacings until a Ψ_A top value is reached, after that thrust density decreases

while thrust-to-power ratio slightly increases. For NACA 0008 and 0006, only the latter behaviour was observed within the considered parameter space: thrust-to-power ratio increases while thrust density decreases for increasing spacing values.

The NACA 0010, which reaches high Θ and Ψ_A at the same time, is compared to the drop profile in Fig. 15 plotting their parametric curves as in Fig. 14. Here the drop profile exhibits a monotonic trend, with decreasing thrust-to-power ratios for increasing thrust densities, in such a way that it is not possible to find a preferential region. However, the low slope of this trend indicates drop collectors as suitable for higher thrust density uses, at the cost of a moderate decrease in thrust-to-power. More generally, this can address further investigation about modified drop profiles, for instance considering elliptic fronts.

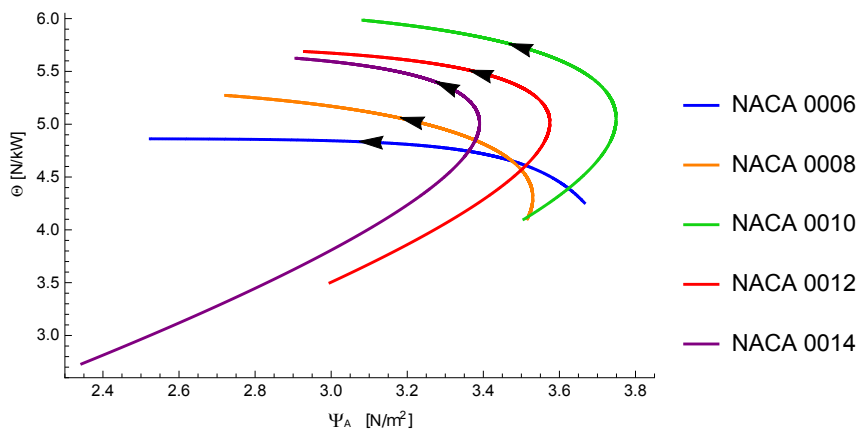


Figure 14: Thrust-to-power ratio vs thrust density diagram for NACA airfoil collectors. Black arrows indicate increasing spacings s .

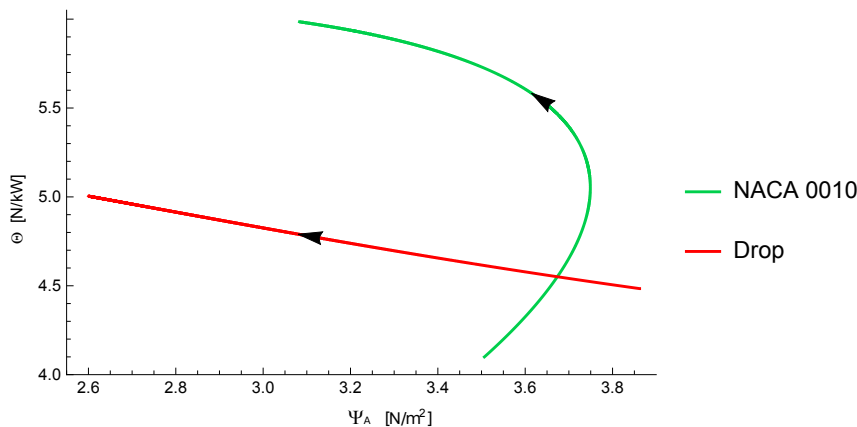


Figure 15: Thrust-to-power ratio vs thrust density diagram for NACA 0010 and drop collectors. Black arrows indicate increasing spacings s .

Figures 15 and 14 show that within the considered parameter space, i.e. for the tested

geometries and spacings, the best performant collector is the NACA 0010, since it gives the best trade-off between thrust-to-power and thrust density.

4. Conclusions

An analysis of different collector electrodes geometries in a EHD thruster has been carried out, estimating performance and providing a comparison between the tested configurations. The parameter space was defined by focusing on collectors shaped as symmetric airfoils, selecting some NACA profiles and a drop profile according to the best literature.

The flow velocity was measured downstream of a parallel set of identical thrusters to approximate a periodic field, revealing that the field of motion remarkably depends on the spacing between units. A close spacing creates channel-like velocity profiles, more affected by the drag phenomenon. Large spacings between adjacent units give velocity fields shaped as double parallel jets, evidencing a partially turbulent behaviour at the Reynolds number of this experiment. A different behaviour was observed for the drop collectors only, which create in this experiment a steady downstream flow, nearly independent of the spacing.

The velocity profiles were used to calculate thrust. Thrust-to-power ratio was determined accounting for the power consumption and this parameter, together with thrust density, was used to assess the performance of the geometries under study.

Within the considered parameter space, i.e. for the tested geometries and spacings, the most interesting characteristics are exhibited by NACA 0010 shaped collectors. These electrodes offer the best compromise between thrust-to-power and thrust density, qualifying as a convenient design choice if both lightness and efficiency are considered. A drop shaped collector with same thickness and chord as the NACA 0010 gave rise to interesting thrust densities at low spacings but did not reach the thrust-to-power ratios of the NACA 0010 geometry. However, the performance of this collector is interesting enough to suggest further investigation about modified versions of this geometry.

The experimental data here obtained could be used both as a baseline for numerical simulations as well as a tool for preliminary EHD thruster design. As a natural development of this work, also further studies on a wider parameter space could be considered, including different geometries with more degrees of freedom for the whole system.

References

- [1] H.-J. Kim, T. Krishna, K. Zeb, V. Rajangam, C. V. V. M. Gopi, S. Sambasivam, K. V. G. Raghavendra, I. M. Obaidat, A comprehensive review of li-ion battery materials and their recycling techniques, *Electronics* 9 (7).
- [2] J. Jean, A. Wang, V. Bulovic, In situ vapor-deposited parylene substrates for ultra-thin, lightweight organic solar cells, *Organic Electronics* 31.

- [3] T. Kadyk, C. Winnefeld, R. Hanke-Rauschenbach, U. Krewer, Analysis and design for fuel cell system for aviation, *Energies* 11 (375).
- [4] G. Matsoukas, N. Ahmed, Experimental investigation of employing asymmetrical electrodes in propulsion of vehicles, *Procedia Eng. - Evolving Energy-IEF International Energy Congress (IEF-IEC2012)* 49 (2012) 247–253.
- [5] A. Ieta, M. Chirita, Electrohydrodynamic propeller for in-atmosphere propulsion; rotational device first flight, *J. Electrostat.* 100 (2019) 103352.
- [6] V. Y. Khomich, I. E. Rebrov, In-atmosphere electrohydrodynamic propulsion aircraft with wireless supply onboard, *J. Electrostat.* 95 (2018) 1–12.
- [7] H. Xu, Y. He, K. L. Strobel, C. K. Gilmore, S. P. Kelley, C. C. Hennick, T. Sebastian, M. R. Woolston, D. J. Perreault, S. R. H. Barrett, Flight of an aeroplane with solid-state propulsion, *Nature* 563 (2018) 532–535.
- [8] N. Monrolin, F. Plouraboué, O. Praud, Electrohydrodynamic thrust for in-atmosphere propulsion, *AIAA J.* 55 (2017) 4296–4305.
- [9] K. Masuyama, S. R. H. Barrett, On the performance of electrohydrodynamic propulsion, *Proc. R. Soc. A* 469 (2154).
- [10] R. S. Vaddi, Y. Guan, A. Mamishev, I. Novosselov, Analytical model for electrohydrodynamic thrust, *Proc. R. Soc. A* 476 (2020) 0220.
- [11] C. K. Gilmore, S. R. H. Barrett, Electrohydrodynamic thrust density using positive corona-induced ionic winds for in-atmosphere propulsion, *Proc. R. Soc. A* 471 (2175).
- [12] H. Xu, Y. He, S. R. H. Barrett, A dielectric barrier discharge ion source increases thrust and efficiency of electroaerodynamic propulsion, *Appl. Phys. Lett.* 114 (254105).
- [13] H. Xu, N. Gomez-Vega, D. R. Agrawal, S. R. H. Barrett, Higher thrust-to-power with large electrode gap spacing electroaerodynamic devices for aircraft propulsion, *J. Phys. D: Appl. Phys.* 53 (2020) 025202 (11pp).
- [14] V. Khomich, V. Malanichev, I. Rebrov, Electrohydrodynamic thruster for near-space applications, *Acta Astronautica* 180 (2021) 141–148.
- [15] F. Canning, C. Melcher, E. Winet, Asymmetrical capacitor for propulsion, NASA CR-2004-213312.
- [16] F. Sottovia, S. Fiorini, M. Belan, F. Maggi, L. Arosti, A new experimental facility for ionic propulsion studies, to appear in: *ICTAM 2020+1, 25th International Congress of Theoretical and Applied Mechanics.*
- [17] L. Zhao, K. Adamiak, Ehd gas flow in electrostatic levitation unit, *J. Electrostat.* 64 (2006) 639–645.

- [18] A. A. Martins, M. J. Pinheiro, Modeling of an ehd corona flow in nitrogen gas using an asymmetric capacitor for propulsion, *J. Electrostat.* 69.
- [19] M. V. Zagarola, A. J. Smits, Mean-flow scaling of turbulent pipe flow, *J. Fluid Mech.* 373 (1998) 33–79.